High-Frequency Irreversible Electroporation for Treatment of Primary Liver Cancer: A Proof-of-Principle Study in Canine Hepatocellular Carcinoma

Brittanie R. Partridge, DVM, Timothy J. O'Brien, PhD, Melvin F. Lorenzo, BS, Sheryl L. Coutermarsh-Ott, DVM, Sabrina L. Barry, DVM, Krystina Stadler, DVM, Noelle Muro, DVM, Mitchell Meyerhoeffer, BS, Irving C. Allen, PhD, Rafael V. Davalos, PhD, and Nikolaos G. Dervisis, DVM, PhD

ABSTRACT

Purpose: To determine the safety and feasibility of percutaneous high-frequency irreversible electroporation (HFIRE) for primary liver cancer and evaluate the HFIRE-induced local immune response.

Materials and Methods: HFIRE therapy was delivered percutaneously in 3 canine patients with resectable hepatocellular carcinoma (HCC) in the absence of intraoperative paralytic agents or cardiac synchronization. Pre- and post-HFIRE biopsy samples were processed with histopathology and immunohistochemistry for CD3, CD4, CD8, and CD79a. Blood was collected on days 0, 2, and 4 for complete blood count and chemistry. Numeric models were developed to determine the treatment-specific lethal thresholds for malignant canine liver tissue and healthy porcine liver tissue.

Results: HFIRE resulted in predictable ablation volumes as assessed by posttreatment CT. No detectable cardiac interference and minimal muscle contraction occurred during HFIRE. No clinically significant adverse events occurred secondary to HFIRE. Microscopically, a well-defined ablation zone surrounded by a reactive zone was evident in the majority of samples. This zone was composed primarily of maturing collagen interspersed with $CD3^+/CD4^-/CD8^-$ lymphocytes in a proinflammatory microenvironment. The average ablation volumes for the canine HCC patients and the healthy porcine tissue were 3.89 cm^3 ± 0.74 and 1.56 cm^3 ± 0.16, respectively ($P = .03$), and the respective average lethal thresholds were 710 V/cm ± 28.2 and 957 V/cm ± 24.4 V/cm ($P = .0004$).

Conclusions: HFIRE can safely and effectively be delivered percutaneously, results in a predictable ablation volume, and is associated with lymphocytic tumor infiltration. This is the first step toward the use of HFIRE for treatment of unresectable liver tumors.

ABBREVIATIONS

ALP = alkaline phosphatase, ALT = alanine aminotransferase, FFPE = formalin-fixed, paraffin-embedded, H&E = hematoxylin and eosin, HCC = hepatocellular carcinoma, HFIRE = high-frequency irreversible electroporation, ICU = intensive care unit, IPA = Ingenuity Pathway Analysis, IRE = irreversible electroporation

From the Departments of Small Animal Clinical Sciences (B.R.P., S.L.B., K.S., N.M., M.M., I.C.A., N.G.D.) and Biomedical Sciences and Pathobiology (S.L.C.-O.), Virginia–Maryland College of Veterinary Medicine, DSACS, Phase II, 205 Duck Pond Drive (0442), Blacksburg, VA 24061; and Department of Biomedical Engineering and Mechanics (T.J.O., M.F.L., R.V.D.), Virginia Tech University, Blacksburg, Virginia. Received May 19, 2019; final revision received October 18, 2019; accepted October 19, 2019. **Address correspondence to** N.G.D.; E-mail: dervisis@vt.edu

B.R.P. and T.J.O. contributed equally to this work.

M.F.L. and R.F.D. have pending and issued patents in the area of irreversible electroporation and may receive royalties. None of the other authors have identified a conflict of interest.

Figures E1 and E2, Tables E1 and E2, and Videos 1 and 2 can be found by accessing the online version of this article on *www.jvir.org* and clicking on the Supplemental Material tab.

J Vasc Interv Radiol 2020; 31:482–491

https://doi.org/10.1016/j.jvir.2019.10.015

As in humans, hepatocellular carcinoma (HCC) is common in canines, in which approximately 60% of HCC cases are surgically resectable. As in humans, nonresectable tumors carry a grave prognosis because of limited effective alternative treatment options (1,2). As canine HCC appears to share many similarities in clinical behavior with HCC in humans, it could service as a model for investigation into novel therapies. More importantly, resectable canine HCC would provide the opportunity to evaluate the effectiveness of local ablative therapy before its use in nonresectable tumors.

The liver is of particular interest because it is an immunologically rich but tolerogenic environment (3). Therefore, local ablative treatment within the liver may be able to activate the immune system, resulting in local and systemic antitumor immune responses. Energy-based focal ablation therapies provide an alternative to surgical resection or radiation therapy. Unlike thermal ablation therapies (radiofrequency, microwave, and cryoablation therapies), irreversible electroporation (IRE) relies on the administration of short, intense, pulsed electric fields to induce nonthermal irrevocable disruption of homeostasis and cell death (4,5). Consequently, this therapy encourages a unique immune response compared with other ablative techniques. More recently, it was shown that IRE could trigger as much as 2–3 times the amount of T cell proliferation in comparison with thermal therapies (6). Despite this exciting revelation, required cardiac synchronization and intraoperative paralytic agents can make IRE procedures somewhat cumbersome (7,8).

High-frequency IRE (HFIRE) could be used to capitalize on these proinflammatory conditions after therapy and minimize the difficulties associated with typical IRE procedures. This next generation of IRE negates the need for cardiac synchronization and paralytic agents by using rapid bipolar pulses that minimize nerve and muscle excitation (9–12). Further, HFIRE therapy has been shown to preferentially target malignant cells in vitro (13,14).

The objective of the present first-in-canine patient pilot study was to determine the feasibility of percutaneous HFIRE for treatment of primary liver cancer and evaluate the immunologic response to the ablation.

MATERIALS AND METHODS

Canine Patients

Client-owned canines diagnosed with HCC were recruited at the Virginia–Maryland College of Veterinary Medicine Teaching Hospital from January 2018 to March 2018. All canines were screened for inclusion with a complete blood count, serum chemistry, urinalysis, prothrombin time, partial thromboplastin time, computed tomography (CT) imaging of the thorax and abdomen with triple-phase contrast enhancement, and ultrasound (US)-guided needle core biopsy of the liver mass before enrollment. Inclusion criteria included the presence of a surgically resectable primary liver tumor, a histologic diagnosis of HCC, and liver enzyme levels lower than 4 times the upper reference limit. Canines were excluded if their tumor was nonresectable based on consultation with a board-certified surgeon or if survival was expected to be less than 6 weeks because of the presence of significant comorbidities. Informed owner consent was obtained before enrollment, and the study was approved by the Virginia Tech institutional animal care and use committee.

Canine Characteristics

Three canines met the inclusion criteria and were enrolled in the study. All canine patients were between 13 and 15 years old and considered geriatric (15).

Canine 1 was a 15-year-old castrated male toy poodle with concurrent diabetes mellitus (controlled), hyperadrenocorticism (untreated), and seizures (controlled) that initially presented for general malaise and in which subsequent bloodwork revealed elevated liver enzyme levels. Magnetic resonance imaging performed after initial diagnosis of HCC revealed a small primary brain tumor in the left frontal lobe most consistent with a meningioma and probable small cerebral hemorrhages.

Canine 2 was a 13-year-old spayed female mixed-breed dog with concurrent hypothyroidism (medically controlled) that was asymptomatic on presentation but in which routine bloodwork revealed significant increases in liver enzyme levels, which initiated a thorough workup.

Canine 3 was a 14-year-old castrated male toy poodle with no significant concurrent medical conditions that presented with clinical signs of anorexia and weight loss.

Imaging

All canines were imaged by using an Aquilion CT scanner (Toshiba, Tokyo, Japan) and were anesthetized via inhalation anesthesia with breath-hold during the scan. Precontrast, immediate, 1-minute delayed, and 3-minute delayed scans of the thorax and abdomen were obtained with the use of iopromide contrast agent (Ultravist; Bayer, Leverkusen, Germany) and a pressure injector (Stellant; Medrad/Bayer). Images were analyzed on a Horos image station. Canines were imaged before HFIRE treatment and 4 days after treatment.

HFIRE Treatment

A custom-built HFIRE generator (EPULSUS-FBM1-5; Energy Pulse Systems, Lisbon, Portugal) capable of producing submicrosecond bipolar pulses in rapid bursts was used to deliver HFIRE therapy via a single 18-gauge bipolar electrode (AngioDynamics, Latham, New York) percutaneously. The generator was set to deliver 300 bursts of a voltage amplitude of 2,250 V via a voltage waveform presenting pulse widths of 2 μs with a 5-μs delay between each change in polarity (on/off/on, 2 μs/5 μs/2 μs) for a total "on" time (ie, energized time) of 100 μs for each burst. An oscilloscope (DPO2002B; Tektronix, Beaverton, Oregon) was used to monitor the voltage and current waveforms

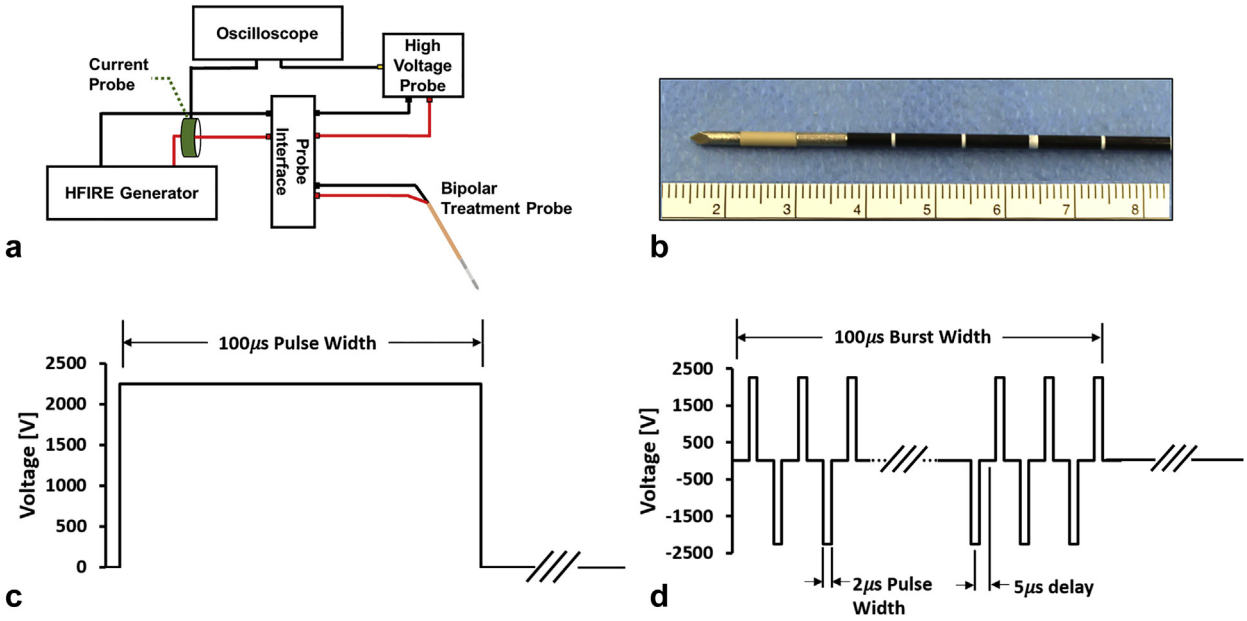

Figure 1. **(a)** Schematic illustration of HFIRE experimental setup and **(b)** 18-gauge bipolar electrode. **(c)** A standard IRE voltage waveform pulse and **(d)** a representative HFIRE voltage waveform (on/off/on, 2 μs/5 μs/2 μs). Twenty-five bipolar pulses contribute to a single HFIRE burst with a burst width of 100 μs.

subsequent to the signal being attenuated with a 1,000× high-voltage probe (P5210A; Tektronix) and passing through a current probe (no. 2877; Pearson Electronics, Palo Alto, California). **Figure 1** illustrates the bipolar electrode, a schematic illustration of the experimental setup, and a comparison between a typical IRE voltage waveform and the HFIRE voltage waveform used in the present study.

HFIRE was delivered with the canines under inhalation general anesthesia without intraoperative paralytic agents and cardiac synchronization. However, canines were monitored continuously with electrocardiography to visualize any potential abnormalities. Each canine was placed on dorsal recumbency, the ventral abdomen hair was clipped with surgical clippers, and surgical aseptic technique was used to advance the sterilized percutaneous HFIRE probe under US guidance. US monitoring continued during the HFIRE treatment.

Numeric Modeling

The HFIRE treatment protocol was designed to ablate a portion of the tumor tissue and elicit an immune response. Therefore, numeric modeling was employed to predict electric field distributions and determine pulsing parameters that result in ablation volumes constrained to portions of the tumor tissue. Accordingly, abdominal CT images from canine HCC patients were imported into 3D Slicer (an open-source platform for medical image informatics), in which relevant anatomic features (liver, hepatic artery, and tumor) were segmented. Then, a surface model maker tool was employed to reconstruct the identified features in 3 dimensions. Each relevant geometry was transferred to 3-matic (Materialse, Leuven, Belgium), in which the bipolar electrode was reconstructed and placed into the simulated tumor tissue model. The entire assembly was meshed for import into a commercial finite element package (COMSOL Multiphysics, version 5.4; COMSOL, Stockholm, Sweden) for analysis.

Dynamic electrical properties were then assigned to normal and malignant tissue within patient-specific hepatic geometries by using tissue data normalized to hepatic tissue properties (16). The methods for predicting electric field distributions for HFIRE are similar to those described for IRE therapies (17–20). The electric field distribution can be derived from **Equation 1** and applying the electroquasistatic approximation:

$$\nabla(\sigma\nabla\Phi) = 0 \qquad \text{(Eq. 1)}$$

where σ is the tissue conductivity and Φ is the electric potential. The electrical boundary conditions at the tissue–electrode interface were set to $\Phi = V$ (source) and $\Phi = 0$ (sink). Boundaries not in contact with an electrode were treated as electrically insulating.

Applying methods adapted from O'Brien et al (21), electrical current measured during therapy were used to establish treatment-specific conductivity curves. Then, the minimum electric field required to induce cell death (ie, the lethal threshold) was determined by comparing the measured volumetric ablation dimensions with those predicted from the numeric model. The electric field that corresponded to the closest matching volumetric dimensions was designated as the lethal threshold.

Siddiqui et al (10) performed an equivalent HFIRE pulsing protocol to healthy porcine liver tissue in their study. Electrical current and lesion volume data from these studies

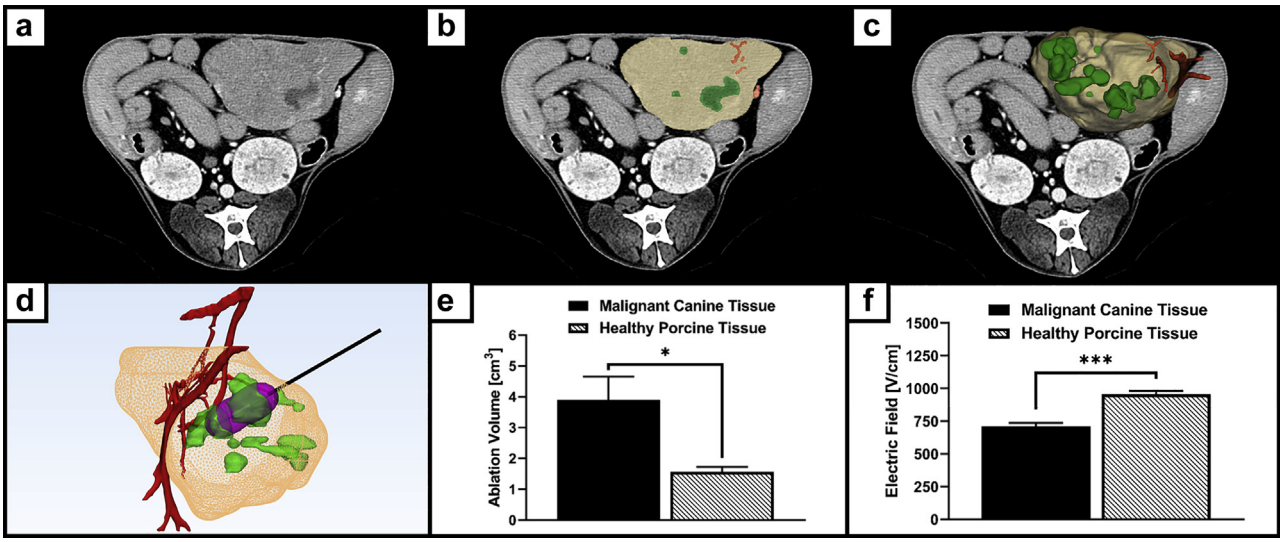

Figure 2. **(a)** Schematic illustration of the 3-dimensional reconstruction and numeric modeling process for canine 1. CT images were imported into 3D Slicer **(a)**, in which the relevant features were highlighted on each CT image **(b)**. A surface maker was then used to interpolate between each slice and reconstruct the identified features in 3 dimensions **(c)**. All relevant features were transferred to 3-matic for assembly with the bipolar electrode and meshing for analysis within COMSOL version 5.4 **(d)**. **(e)** The average ablation volumes for the malignant canine patients and the healthy porcine tissue were 3.89 cm^3 ± 0.74 and 1.56 cm^3 ± 0.16, respectively ($P = .03$), and **(f)** the respective average lethal thresholds were 710 V/cm ± 28.2 and 957 V/cm ± 24.4 ($P = .0004$).

were employed, facilitating a treatment-specific comparison of lethal thresholds for healthy and malignant tissue. **Figure 2** illustrates each step of the 3-dimensional reconstruction process for the patient-specific model, as well as a comparison between diseased and healthy hepatic tissue electric field thresholds. Details on numeric modeling are accessible in **Table E1** (available online on the article's Supplemental Material page at *www.jvir.org*) in conjunction with the material properties applied.

Canine Patient Hospitalization and Tumor Resection

All canines were hospitalized after HFIRE therapy in the intensive care unit (ICU) for monitoring until surgical resection of their HCC. The surgery was performed 4 days after HFIRE treatment, immediately after the second CT scan. Tumor resection was performed by using standard surgical technique. After surgery, the tumor was submitted for histopathologic and immunohistochemical analysis. Canines were recovered in the ICU and discharged to their owners 2 days later. Recheck examinations and blood collections were performed 2 weeks after surgical removal (day 14). Complete blood count and serum chemistry analyses were performed on blood collected at each time point.

Histopathology and Immunohistochemistry

Pre-HFIRE therapy core needle biopsy specimens and post-HFIRE resected tumor samples were processed within 20 minutes of excision. Resected tumor sections were evaluated by a board-certified pathologist (S.L.C.-O.) to confirm a definitive diagnosis and assess completeness of excision. Post-HFIRE samples were grossly examined to identify regions of electroporation, nontreated tumor, and normal nonneoplastic liver. Foci of electroporation were grossly identified in the majority of samples as well-demarcated foci of hemorrhage and necrosis. Sections were taken through these areas for examination of the treated/untreated interface. Sections were routinely processed and stained with hematoxylin and eosin (H&E). Immunohistochemistry for CD3 (rabbit polyclonal, anti-human; A0452; Agilent/Dako, Santa Clara, California), CD4 (rabbit polyclonal, anti-human; NBP1-19371; Novus Biologicals, Littleton, Colorado), CD8 (rabbit polyclonal, anti-human; ab4055; Abcam, Cambridge, United Kingdom), and CD79a (mouse monoclonal, anti-human; CM 067 A, C; Biocare Medical, Pacheco, California) was performed to evaluate the local immune response to treatment. All antibodies were validated and run on a Ventana Benchmark XP automated stainer (Roche Ventana, Oro Valley, Arizona) using the Discovery Universal secondary antibody (760-4205; Roche, Basel, Switzerland), ultraView Universal Alkaline Phosphatase Red Detection Kit (Roche), and hematoxylin counterstain. All antibodies were verified to work in canine tissue before use in research samples (**Fig E1** [available online on the article's Supplemental Material page at *www.jvir.org*]). Lymphocytic infiltration was subjectively quantified for comparison between pre- and posttreatment tumor samples.

Gene Expression Analysis

Formalin-fixed, paraffin-embedded (FFPE) pre- and post-HFIRE treatment tumor tissue was used in a "super array" to compare specific gene expression between pretreatment

and posttreatment tissue. A custom canine-specific super array developed and validated in-house was used, based on the reverse transcriptase (RT)^2 profiler platform (Qiagen, Hilden, Germany). The array design contains 89 genes associated with inflammation and cancer (**Table E2** [available online on the article's Supplemental Material page at *www.jvir.org*]), 3 positive controls (actin, HPRT1, GAPDH), a genomic DNA control, a no-template control, a no-RT control, and a no-amplification control. Sections of the pretreated tumor and of the transition zone at the ablated/nonablated tumor of the posttreatment tumor were selected for RNA extraction. Total RNA was extracted from 10-μm-thick slices of each pretreatment tumor biopsy sample and posttreatment FFPE tissue. RNA extraction was performed by using a Zymo kit according to the manufacturer's directions (Zymo, Irvine, California).

Gene expression on each array was evaluated following the manufacturer's standard protocols. Briefly, the extracted RNA was quantified and assessed through standard quality assurance/quality control. The resulting RNA samples went through first-strand synthesis and quantitative polymerase chain reaction amplification in an ABI 7500 FAST thermocycler (Applied Biosystems, Foster City, California) according to the Qiagen RT^2 profiler protocol. The quantitative RT polymerase chain reaction data were analyzed by using the common ΔΔCt methodology. The pretreatment gene expression profile was compared to the posttreatment group samples, with archived FFPE normal liver tissue from 12 young canine patients of various breeds with congenital portosystemic shunts used for selecting housekeeping genes. Normal liver tissue was collected at the time of surgical correction. The super array results were analyzed by using the GeneGlobe Data Analysis software suite (Qiagen) for individual gene expression differences and Ingenuity Pathway Analysis (IPA) software for pathway analysis. More specifically, Ct values were exported and uploaded to a data analysis Web portal (*http://www.qiagen.com/geneglobe*). Samples were assigned to controls and test groups. Ct values were normalized based on manual selection of reference genes that demonstrated small changes in gene expression (Ct value differences less than 1). The data analysis Web portal calculates fold change/regulation using the ΔΔCt method, in which delta Ct is calculated between gene of interest and an average of housekeeping genes, followed by ΔΔCt calculations. Fold change is then calculated by using the $2^{(-1*\Delta\Delta Ct)}$ formula. All data were ranked and evaluated based on *z*-score as previously described (22).

Statistical Analysis

A total of 3 canine patients with HCC were treated, with 1 treatment performed per patient (total N = 3). Further, a total of 3 healthy pigs were treated, with 1 treatment performed per pig (total N = 3). Data for each are presented as mean values ± standard deviation of the mean. A 2-tailed Student *t* test was performed to determine if the ablation volumes and/or electric field thresholds were significantly different from each other. All statistical analysis was performed within JMP Pro version 14.0.0 (SAS, Cary, North Carolina).

RESULTS

Ablation Volumes and Numerically Determined Lethal Thresholds

CT images taken before HFIRE treatment and 4 days after treatment indicated an average ablation volume of 3.89 cm^3 ± 0.74. In comparison, the average ablation volume for healthy porcine tissue was 1.56 cm^3 ± 0.16 (N = 3 for both treatment groups; $P = .03$; **Fig 2e**) (10,16). The average lethal thresholds for the HCC canine tissue and the healthy porcine tissue were 710 V/cm ± 28.2 and 957 V/cm ± 24.4, respectively (N = 3 for both treatment groups; $P = .0004$; **Fig 2f**). These results are in agreement with previous findings that suggest that HFIRE therapy may preferentially target malignant cells (13). However, more studies would be required to allow any robust conclusions to be made about HFIRE therapies preferentially targeting malignant cells.

Feasibility and Safety of HFIRE Ablation

No clinically significant adverse events were associated with HFIRE treatment. No detectable cardiac interference occurred during HFIRE delivery, and only minimal muscle contraction was noted in the absence of paralytic agents (**Videos 1** and **2** [available online on the article's Supplemental Material page at *www.jvir.org*]). HFIRE resulted in an ablation volume that was visible as predicted by the numeric modeling on CT before surgical resection (day 4) and in gross tumor samples following tumor excision in all 3 canines. Histopathologic analysis revealed a well-defined ablation/tumor interface following HFIRE in 2 canines and poorly defined ablation/tumor interface in a single canine (**Fig 4**).

Hepatotoxicity Assessment

Alanine aminotransferase (ALT) and alkaline phosphatase (ALP) levels both increased compared with baseline following HFIRE treatment (day 0) but resolved over time following tumor removal on day 4 (**Fig 5**). These enzyme elevations were most severe in canine 3 at all time points. No other liver-associated enzymes or hepatobiliary markers were elevated over baseline, and no clinical signs associated with HFIRE treatment were noted during the canines' hospitalization in the ICU. Canine 1 was euthanized 8 days after surgery because of uncontrolled seizures attributed to the animal's brain lesions, so recheck liver values were not available. Canines 2 and 3 were alive at the time of manuscript preparation more than 12 months later and undergo chest radiography and abdominal US every 3 months for disease restaging. Neither recurrence nor

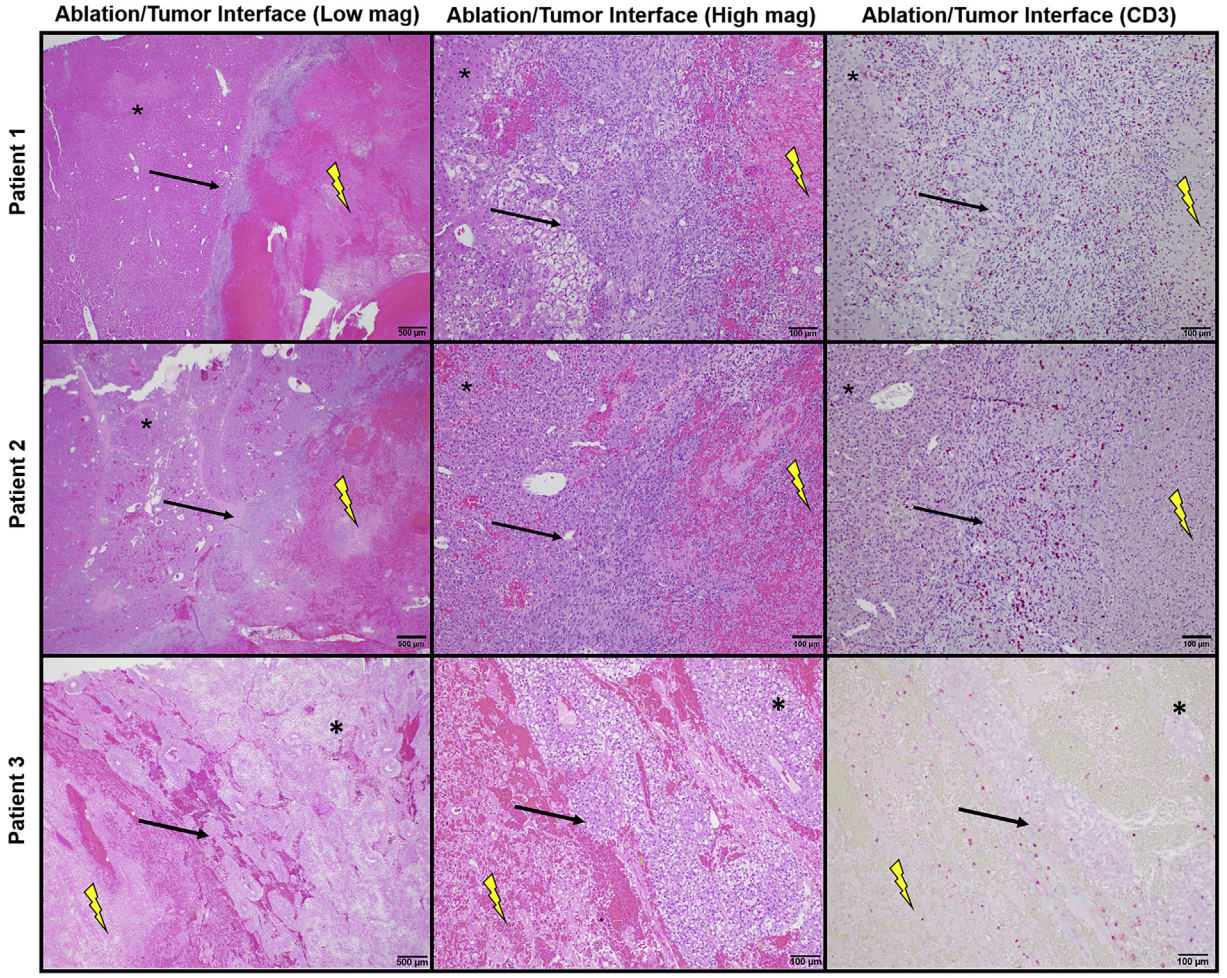

Figure 3. Tumor histopathologic specimens from canine 1 (top) and canine 2 (middle) show the well-defined ablation/tumor interface (arrows) with H&E stain at 40× (left) and 100× (center) magnifications. Immunohistochemistry for CD3 revealed positive (red) staining cells infiltrating the tumor/ablation interface. Canine 3 (bottom) showed absence of a well-defined ablation/tumor interface (arrows) with H&E stain at 40× (left) and 100× (center) magnifications. Immunohistochemistry for CD3 (right) shows the lack of $CD3^+$ cells within the ablation/tumor interface. Positively stained cells are red. Untreated HCC is denoted by asterisks and the ablation tumor volume by lightning bolts.

metastasis has been identified in either canine to date (> 12 mo after treatment).

Immunologic Reaction to the Ablation

Immunohistochemistry on the tumor/ablation interface revealed subjectively increased infiltration with $CD3^+$ lymphocytes following HFIRE treatment in 2 canines (Fig 3) compared with pretreatment samples. Figure E2 (available online on the article's Supplemental Material page at *www.jvir.org*) provides a visual comparison of the $CD3^+$ infiltration before and after treatment. Posttreatment samples were negative for $CD4^+$ and $CD8^+$ cells, suggesting that the infiltrating T cell had a unique $CD3^+/CD4^-/CD8^-$ phenotype (Fig 4). $CD3^+$ lymphocyte infiltration was absent in the canine with a poorly defined ablation/tumor interface (Fig 3). In all canines, the tumor/ablation interface was negative for $CD79a^+$ lymphocytes.

Gene expression analysis indicated up-regulation of 21 genes associated with inflammation and activation of the innate and adaptive immune system following HFIRE treatment in all 3 canines. In contrast, gene expression of 29 genes associated with modulation and regulation of the immune system was downregulated following HFIRE treatment in all 3 canines compared with baseline. Table 1 presents the details of these findings. Further, pathway analysis indicated a specific proinflammatory signaling microenvironment in canines 1 and 2, which corresponds with the $CD3^+$ cell infiltrations, whereas canine 3 lacked this microenvironmental niche (Fig 6a–c). IPA network analysis identified 2 functional networks that fit the canonic pathways identified, cell injury/death and cell-mediated immunity (Fig 6d,e). Both of these networks were significantly upregulated in all canines following HFIRE treatment. However, it should be noted that the data of canine 3 within the networks was actually a significant downregulation moving toward lesser downregulation. Figure 6f shows that NF-κB signaling was one of the most dominant pathways impacted by HFIRE treatment. Gene expression patterns revealed a significant global up-regulation in NF-κB signaling.

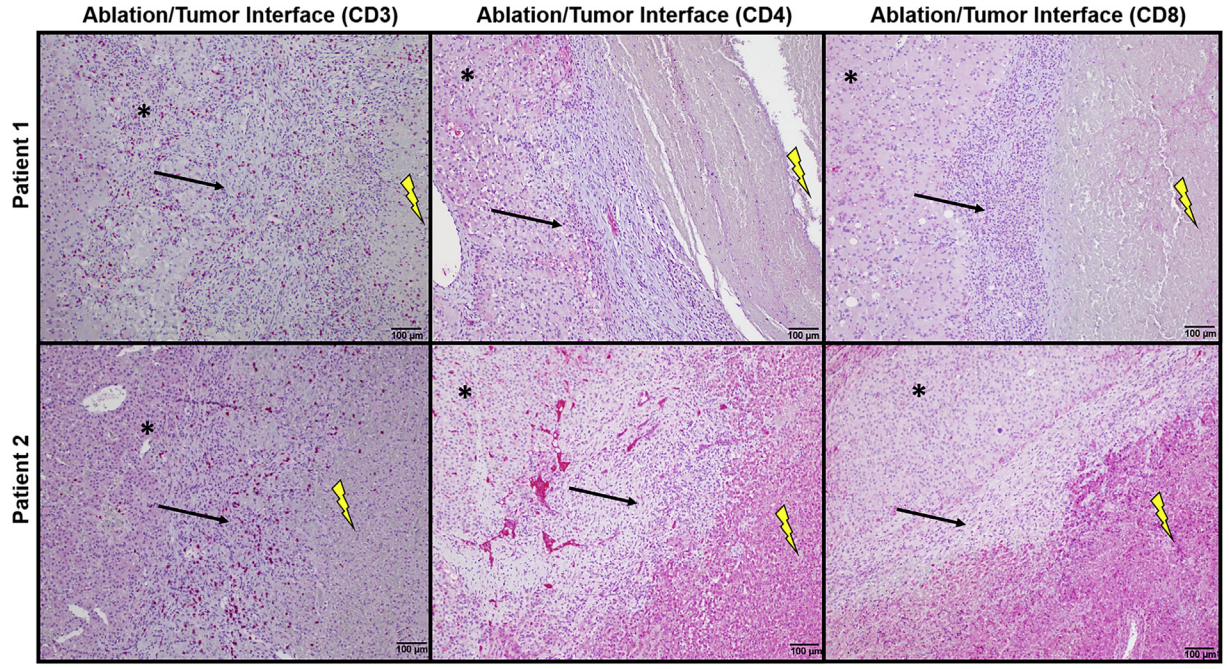

Figure 4. Immunohistochemistry for CD3 (left), CD4 (center), and CD8 (right) on tumor samples from canine 1 (top) and canine 2 (bottom) show infiltration of the ablation/tumor interface (arrows) with $CD3^{+}/CD4^{-}/CD8^{-}$ lymphocytes. Positively stained cells are red, but positive staining in the ablation zone is the result of cross-reaction with dead tissue rather than positive cells. Untreated HCC is denoted by asterisks and the ablation zone by lightning bolts.

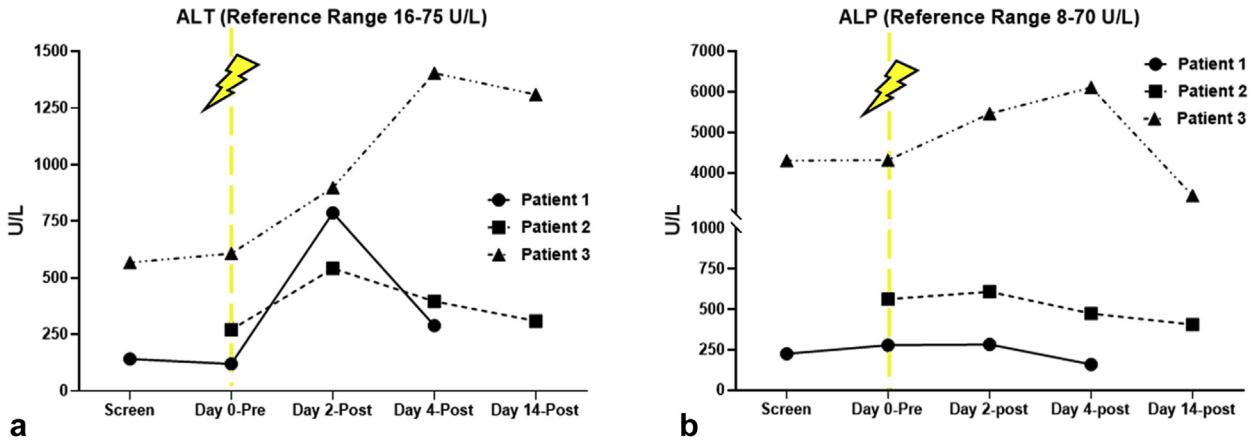

Figure 5. **(a)** ALT and **(b)** ALP levels increased following HFIRE treatment (dashed line and lightning bolt) but resolved over time following tumor removal (day 4).

DISCUSSION

The present proof-of-principle study was designed to determine if HFIRE therapy, delivered percutaneously, could produce rapid, predictable ablations in the absence of intraoperative paralytic agents and cardiac synchronization within a spontaneous canine liver tumor model. A treat-and-resect procedure was established to minimize any risk to the treated animals while also permitting a thorough evaluation of the ablated tissues and the locoregional microenvironment via removal of the entire tumor after therapy.

Energy-directed, minimally invasive procedures have been shown to activate an immune response to enhance cancer cell destruction. Recent in vitro studies have shown IRE to be more influential in comparison with thermal therapies (6). However, the requirement of intraoperative paralytic agents and cardiac synchronization for all IRE procedures can be an impediment, adding more complexity to the modality (7,8). HFIRE therapy, a next-generation IRE therapy, can be safely applied in the absence of intraoperative paralytic agents and cardiac synchronization required during traditional IRE (12,23). Additionally, IRE

and HFIRE therapies alike can, at times, benefit from multiple-electrode (≥ 2 electrodes) configurations when attempting to encompass a large or irregularly shaped tumor. The precise placement and alignment of the electrodes to ensure the intended treatment conditions can be technically challenging and time-consuming. However, a single-needle bipolar treatment probe can alleviate these concerns and provide additional advantages, including percutaneous treatment delivery.

Throughout the present study, percutaneous HFIRE therapy was delivered in the absence of intraoperative paralytic agents and cardiac synchronization, resulting in predictable ablation volumes without any discernable muscle twitch or effect on cardiac function for all 3 canine patients. Consistent with previous findings (10,21), these results indicate the potential of a more precise treatment plan before the ablation of entire tumors.

Table. Mean (n = 3) Fold Change in Gene Expression following HFIRE Treatment Compared with Baseline

Gene Name	Average ΔCt	ΔΔCt	Fold Change
SPP1	8.464517	0.002831	87.14
IL1R2	7.04305	0.007583	26.01
CCR5	11.26715	0.000406	20.51
IL18	9.43465	0.001445	16.56
TLR2	10.772517	0.000572	15.97
IL15	7.468417	0.005647	8.96
CSF1	10.111217	0.000904	6.63
CCL13	9.357183	0.001525	6.42
EGF	10.152517	0.000879	4.08
MYC	3.36785	0.096867	3.94
EGFR	5.224617	0.026744	3.84
ICAM1	2.849117	0.138781	3.84
CCL4	5.573083	0.021006	3.31
IFNG	11.26715	0.000406	2.9
IL13	7.092483	0.007327	2.77
PTGS2	8.85675	0.002157	2.77
TLR3	2.682717	0.155748	2.55
CCL20	9.81035	0.001114	2.42
FOXP3	8.36055	0.003042	2.28
LAMP1	1.988017	0.252085	2.19
MYD88	5.736417	0.018757	2.01
CCR2	5.956783	0.0161	−2.38
IL10	9.812583	0.001112	−2.91
CD244	9.75245	0.001159	−3.04
TGFB1	5.669317	0.01965	−3.05
CXCL8	6.082583	0.014756	−3.31
BCL2	9.523883	0.001358	−3.56
IGF1	9.51565	0.001366	−3.58
IL6	9.448917	0.001431	−3.75
PDCD1LG2	7.441417	0.005753	−3.76
CCR10	8.127617	0.003576	−3.78
IL23A	9.336483	0.001547	−4.05
IL1A	9.23725	0.001657	−4.34
GZMB	8.733317	0.00235	−4.45
CCR7	9.102383	0.001819	−4.76
CD274	8.996317	0.001958	−5.13
CXCR4	8.713083	0.002383	−6.24
TLR7	8.38755	0.002986	−7.82
IL1R1	7.95095	0.004041	−10.58
IL5	7.800917	0.004484	−11.74
CCR1	7.69145	0.004838	−12.67
TNF	7.35655	0.006102	−15.98
JAK1	3.030883	0.122353	−16.31
APLNR	1.164283	0.446186	−23.79
BCL2L1	4.872617	0.034135	−31.5
HIF1A	2.21625	0.2152	−51.9
STAT3	4.721617	0.037901	−99.25
CCL2	4.523183	0.04349	−113.88
NFKB1	4.19035	0.054775	−143.43
CXCL10	2.251117	0.210061	−381.67

Note–Only genes with significant changes in expression are shown, ranked from increased to decreased expression.
ΔCt = difference between Ct value of gene of interest and Ct of the housekeeping gene; ΔΔCt = relative fold gene expression of samples when performing real-time polymerase chain reaction; HFIRE = high-frequency irreversible electroporation.

The immunologic reaction analysis provided a unique $CD3^+/CD4^-/CD8^-$ phenotype of lymphocytes infiltrating the ablation/tumor interface. This was somewhat unexpected, as terminally differentiated T cells typically express either CD4 or CD8. Double-negative T lymphocytes appear to be involved in immune regulation and tolerance, as well as host defense and inflammation (24–26). As the liver is an immunologically rich but active organ, the presence of these cells may serve a role in tumor antigen recognition in response to the neoplastic cell death after HFIRE. However, canine 3 did not present a clear reactive zone histologically. In addition, there was minimal lymphocytic infiltration, and the microenvironment as assessed via the super array was distinct when compared with the other 2 canines. Despite the abundant necrosis contained within this canine's tumor, adaptive immune cell infiltration was not detected. Additionally, because of the amount of necrosis associated with this tumor, it was difficult to appreciate the ablation zone grossly, so it is possible that sections submitted for histopathologic examination did not represent the ablation/tumor interface.

A hepatotoxicity assessment indicated that liver enzymes (ALT and ALP) increased above baseline levels in all canines following HFIRE treatment and resolved following tumor removal. This increase was anticipated, as tumor cells and normal hepatocytes likely contain similar enzymes that are released upon cell death. Canine 3 had the most severe liver enzyme elevations and the longest time for these elevations to resolve, likely secondary to the relative increased tumor size compared with canines 1 and 2.

A unique transition zone surrounding the tumor-ablated volume was observed in 2 of the 3 treated canine patients.

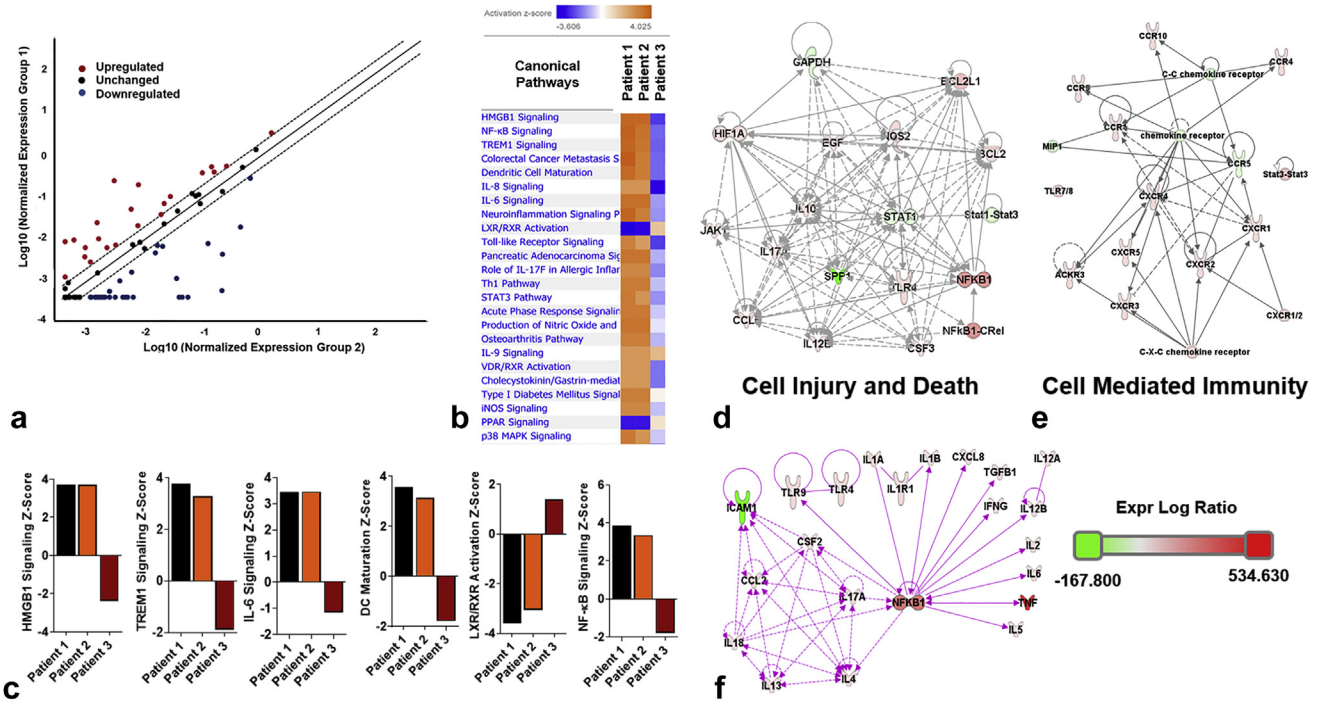

Figure 6. **(a)** Scatterplot of gene expression array data illustrating the results from Table 1. Twenty-two gene expressions were significantly up-regulated and 29 were significantly down-regulated following HFIRE treatment in all 3 canines compared with baseline. Change in expression of all other genes was less than 2-fold (unchanged) and represented by the solid black line. **(b)** IPA of global changes in gene expression patterns following HFIRE revealed diverse but functionally related predications in canonic pathways significantly increased by HFIRE for canines 1 and 2. Conversely, the gene expression profile for canine 3 showed no change or down-regulation of functionally similar canonic pathways. **(c)** The top 6 canonic pathways impacted by HFIRE, comparing pretreatment versus posttreatment, ranked by *z*-score. Canines 1 and 2 are highly consistent, with canine 3 exhibiting opposing results. Pathways associated with the activation of cellular immunity and cell death are significantly upregulated following HFIRE treatment. **(d,e)** IPA network analysis identified 2 functional networks that fit the canonic pathways identified, cell injury/death and cell-mediated immunity. Both of these networks were significantly upregulated in all canines following HFIRE treatment. However, the data from canine 3 within the network were actually a significant downregulation moving toward lesser downregulation. **(f)** NF-κB signaling was one of the most dominant pathways impacted by HFIRE treatment. Gene expression patterns revealed a significant global up-regulation in NF-κB signaling.

This transition zone was characterized by a specific T cell infiltration in a tumor microenvironment of proinflammatory signaling. This response to HFIRE may indicate a unique HFIRE/immune interaction, potentially specific to the liver neoplastic niche. Again, canine 3 lacked the transition zone and the proinflammatory response to HFIRE ablation, which could represent a biologic variant to this ablation technique or an inability of the technique to induce such a response to relatively more necrotic tumor.

The treatment-specific numeric modeling provided lethal threshold estimates for malignant canine and healthy porcine liver tissue. These preliminary outcomes suggest a preferential targeting of malignant cells when applying HFIRE therapy, but more work is required before any conclusions are made.

A major limitation of the present study is its small sample size (N = 3); however, this study was designed to be a proof-of-principle study assessing the safety and feasibility of HFIRE therapy. Comparison of lymphocytic infiltration between pre- and posttreatment tumor samples was subjective, so statistical significance could not be determined. Additionally, multiplexed IHC was not performed on tumor samples, so the conclusion that infiltrating $CD3^+$ cells are also negative for CD4 and CD8 cannot be made. Another limitation is the presence of background staining occurring in the CD4 and CD8 samples. CD4 and CD8 cross-react with dead tissue, so the ablation zone was heavily stained in most samples, further complicating interpretation. Flow cytometry on cells isolated from the ablation/tumor interface may confirm the phenotype of infiltrating cells and is currently under way.

HFIRE therapy can be safely delivered percutaneously with a predictable ablation volume. This minimally invasive ablative procedure may be associated with unique lymphocytic tumor infiltration ($CD3^+/CD4^-/CD8^-$) and may potentially elicit preferential therapeutic targeting toward malignant cell types.

ACKNOWLEDGMENTS

The present study was supported by the Veterinary Memorial Fund, Institute for Critical Technology and Applied Science Center for Engineered Health, Pancreatic Cancer Action Network (PanCAN) Grant PanCAN 16-65-IANN, and the Grayton Friedlander Memorial Fund. The authors thank members of the Veterinary Teaching Hospital (VTH)

Oncology service (Klahn, Olsen, and Wyne), VTH Radiology service (Stadler), VTH Surgery service (Muro), VTH Anesthesia (Carpenter), Dr. Coy Allen's laboratory (Ringel-Scala and Brock), Dr. John Rossmeisl's laboratory (Arena), and Anne Avery at CSU's Clinical Immunology Lab for all of their contributions to this project.

REFERENCES

1. Balogh J, Victor D III, Asham EH, et al. Hepatocellular carcinoma: a review. J Hepatocell Carcinoma 2016; 3:41–53.
2. Liptak JM, Dernell WS, Monnet E, et al. Massive hepatocellular carcinoma in dogs: 48 cases (1992–2002). J Am Med Vet Assoc 2004; 225: 1225–1230.
3. Robinson MW, Harmon C, O'Farrelly C. Liver immunology and its role in inflammation and homeostasis. Cell Mol Immunol 2016; 13:267–276.
4. Davalos RV, Mir LM, Rubinsky B. Tissue ablation with irreversible electroporation. Ann Biomed Eng 2005; 33:223–231.
5. Edd JF, Horowitz L, Davalos RV, Mir LM, Rubinsky B. In vivo results of a new focal tissue ablation technique: irreversible electroporation. IEEE Trans Biomed Eng 2006; 53:1409–1415.
6. Shao Q, O'Flanagan S, Lam T, et al. Engineering T cell response to cancer antigens by choice of focal therapeutic conditions. Int J Hyperthermia 2019; 36:1–9.
7. Ball C, Thomson KR, Kavnoudias H. Irreversible electroporation: a new challenge in 'out of operating theater' anesthesia. Anesth Analg 2010; 110:1305–1309.
8. Nielsen K, Scheffer HJ, Vieveen JM, et al. Anaesthetic management during open and percutaneous irreversible electroporation. Br J Anaesth 2014; 113:985–992.
9. Arena CB, Sano MB, Rossmeisl JH Jr, et al. High-frequency irreversible electroporation (H-FIRE) for non-thermal ablation without muscle contraction High-frequency irreversible electroporation (H-FIRE) for non-thermal ablation without muscle contraction. Biomed Eng Online 2011; 10:102.
10. Siddiqui IA, Latouche EL, DeWitt MR, et al. Induction of rapid, reproducible hepatic ablations using next-generation, high frequency irreversible electroporation (H-FIRE) in vivo. HPB 2016; 18:726–734.
11. Miklovic T, Latouche EL, DeWitt MR, Davalos RV, Sano MB. A comprehensive characterization of parameters affecting high-frequency irreversible electroporation lesions. Ann Biomed Eng 2017; 45: 2524–2534.
12. Sano MB, Fan RE, Cheng K, et al. Reduction of muscle contractions during irreversible electroporation therapy using high-frequency bursts of alternating polarity pulses: a laboratory investigation in an ex vivo swine model. J Vasc Interv Radiol 2018; 29:893–898.e4.
13. Ivey JW, Latouche EL, Sano MB, Rossmeisl JH, Davalos RV, Verbridge SS. Targeted cellular ablation based on the morphology of malignant cells. Sci Rep 2015; 5:1–17.
14. Ivey JW, Bonakdar M, Kanitkar A, Davalos RV, Verbridge SS. Improving cancer therapies by targeting the physical and chemical hallmarks of the tumor microenvironment. Cancer Lett 2016; 380:330–339.
15. Moore AS, Frimberg AE. Usefulness of chemotherapy for the treatment of very elderly dogs with multicentric lymphoma. J Am Vet Med Assoc 2018; 252:852–859.
16. Hasgall PA, Di Gennaro F, Baumgartner C, et al. *IT'IS Database for thermal and electromagnetic parameters of biological tissues, version 4*. 2018.
17. Edd JF, Davalos RV. Mathematical modeling of irreversible electroporation for treatment planning. Technol Cancer Res Treat 2007; 6:275–286.
18. Garcia PA, Pancotto T, Rossmeisl JH Jr, et al. Non-thermal irreversible electroporation (N-TIRE) and adjuvant fractionated radiotherapeutic multimodal therapy for intracranial malignant glioma in a canine patient. Technol Cancer Res Treat 2011; 10:73–83.
19. Garcia PA, Rossmeisl JH, Neal RE, Ellis TL, Davalos RV. A parametric study delineating irreversible electroporation from thermal damage based on a minimally invasive intracranial procedure. Biomed Eng. Online 2011; 10:34.
20. Latouche EL, Sano MB, Lorenzo MF, Davalos RV, Martin RCG. Irreversible electroporation for the ablation of pancreatic malignancies: a patient-specific methodology. J Surg Oncol 2017; 115:711–717.
21. O'Brien TJ, Passeri M, Lorenzo MF, et al. Experimental high-frequency irreversible electroporation using a single-needle delivery approach for nonthermal pancreatic ablation in vivo. J Vasc Interv Radiol 2019; 30: 854–862.e7.
22. Ringel-Scaia VM, Beitel-White N, Lorenzo MF, et al. High-frequency irreversible electroporation is an effective tumor ablation strategy that induces immunologic cell death and promotes systemic anti-tumor immunity. EBioMedicine 2019; 44:112–125.
23. Arena CB, Sano MB, Rossmeisl JH Jr, et al. High-frequency irreversible electroporation (H-FIRE) for non-thermal ablation without muscle contraction. Biomed Eng Online 2011; 10:102.
24. Martina MN, Noel S, Saxena A, Rabb H, Hamad ARA. Double negative (DN) αβ T cells: misperception and overdue recognition. Immunol Cell Biol 2015; 93:305–310.
25. D'Acquisto F, Crompton T. CD3+CD4−CD8− (double negative) T cells: saviours or villains of the immune response? Biochem. Pharmacol 2011; 82:333–340.
26. Ford MS, Young KJ, Zhang Z, Ohashi PS, Zhang L. The immune regulatory function of lymphoproliferative double negative T cells in vitro and in vivo. J Exp Med 2002; 196:261–267.

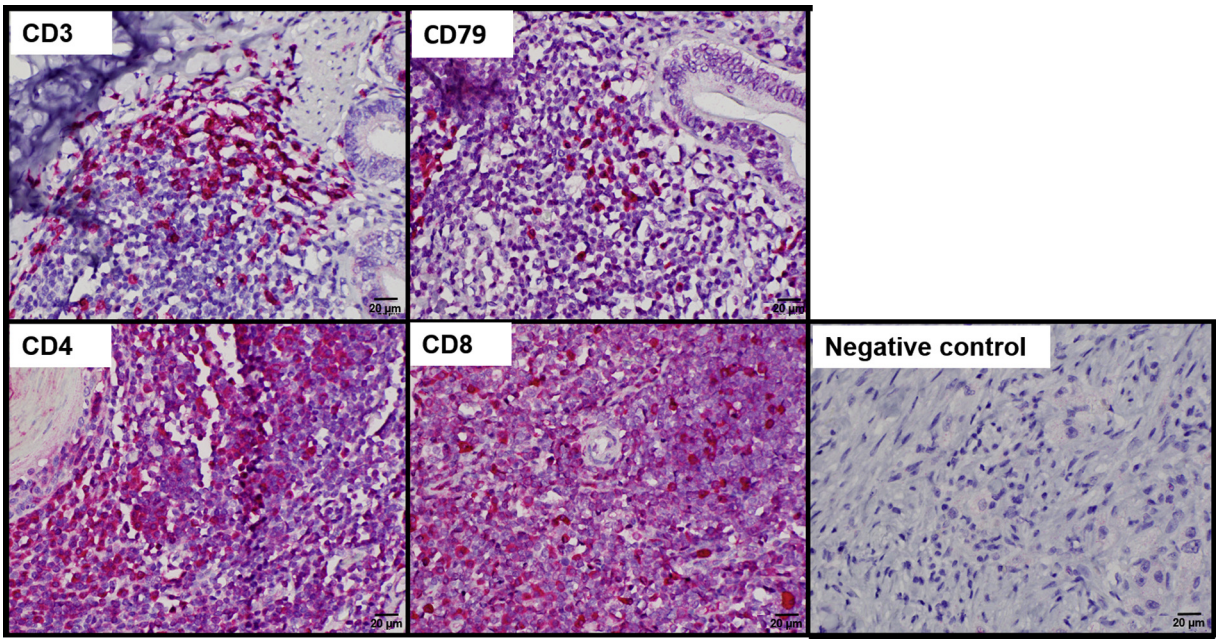

Figure E1. All antibodies were validated in canine tissue before use in research samples by using a Ventana Benchmark XP automated immunohistochemical stainer (Roche Ventana, Oro Valley, Arizona) with ultraView Universal Alkaline Phosphatase Red Detection Kit (Roche, Basel, Switzerland) and hematoxylin counterstain. For all antibodies, positive cells are characterized by abundant, diffuse, cytoplasmic red stain. The CD4 and CD8 stains do exhibit a slight increase in background staining, which was taken into account when evaluating research samples. All images are taken at 40× magnification. Tissues used for positive controls are as follows: CD3 and CD79a-intestinal lymphoid tissue, CD4 and CD8-tonsil.

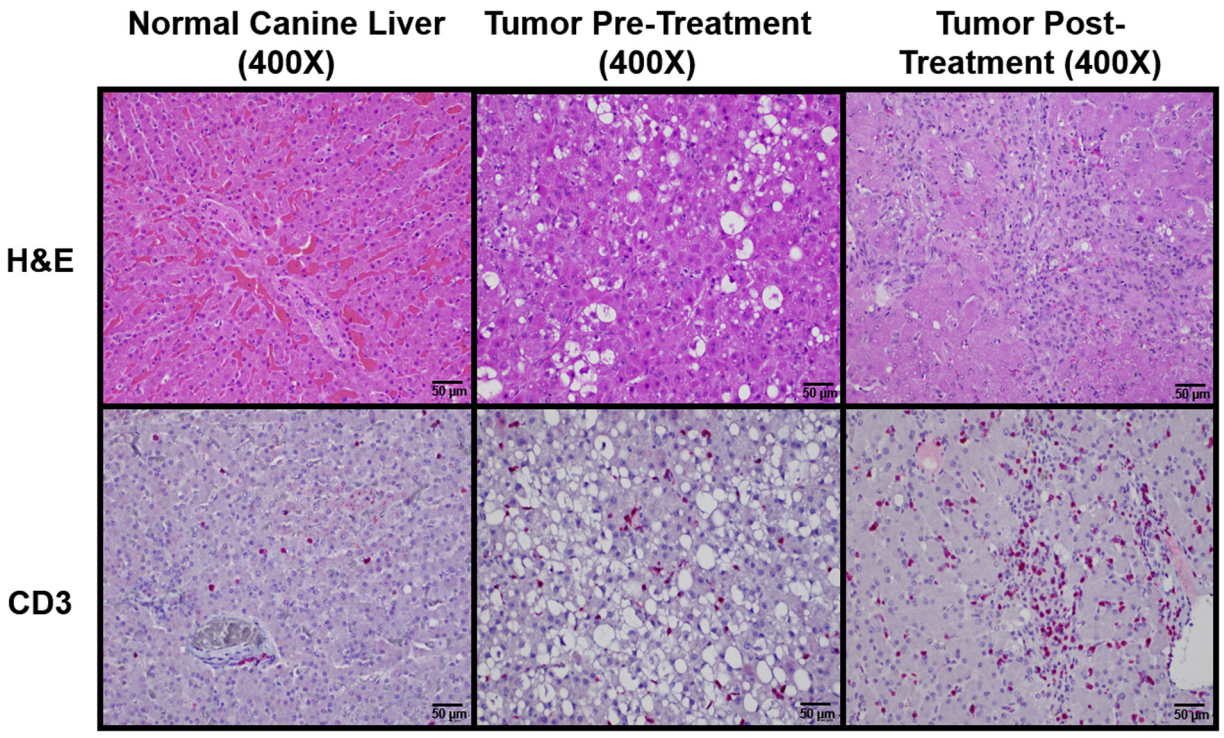

Figure E2. Top: Histopathologic samples with hematoxylin and eosin stain of normal canine liver (left), pretreatment tumor samples (middle), and posttreatment tumor samples (right) showing disruption of normal liver architecture and infiltration of inflammatory cells after treatment. Bottom: Immunohistochemistry for CD3 in normal canine liver (left), pretreatment tumor samples (center), and post-treatment tumor samples (right) showing an increase in infiltration of positive staining cells (red) in the posttreatment tumor samples compared with pretreatment and normal liver samples.

Table E1. Tissue and Electrode Properties Employed for Numerical Modeling

Material/ Parameter	Value	Units	Ref.
Liver			
ρ, Density	1,079	kg/m^3	16
c_p, Heat capacity	3,540	*J/kg/K*	16
k, Thermal conductivity	0.52	*W/m/K*	16
α, Thermal coefficient of conductivity	2	%/°C	16
ω_b, Perfusion	$7.15e^{-3}$	1/s	16
σ_0, Initial electrical conductivity	0.221	*S/m*	–
A, Multiplier	1.25	–	–
E_{del}, Center of transition zone	1,000	V/cm	21
E_{range}, One half of transition range	700	V/cm	21
Electrode			
ρ, Density	7,900	kg/m^3	16
c_p, Heat capacity	500	*J/kg/K*	16
k, Thermal conductivity	15	*W/m/K*	16
α, Electrical conductivity	$2.22e^{-6}$	*S/m*	16

Table E2. List of 89 Genes of Interest That Were Associated with Inflammation and Cancer

Gene Symbol	RefSeq No.	Gene Name
ACKR3	NM_001003281	chemokine (C-X-C motif) receptor 7
AICDA	NM_001003380	activation-induced cytidine deaminase
BCL2	NM_001002949	B-cell CLL/lymphoma 2
BCL2L1	NM_001003072	BCL2-like 1
CCL2	NM_001003297	chemokine (C-C motif) ligand 2
CCL20	NM_001005254	chemokine (C-C motif) ligand 20
CCL28	NM_001005257	chemokine (C-C motif) ligand 28
CCL4	NM_001005250	chemokine (C-C motif) ligand 4
CCL5	NM_001003010	chemokine (C-C motif) ligand 5
CCR1	NM_001038606	chemokine (C-C motif) receptor 1
CCR10	XM_844228	chemokine (C-C motif) receptor 10
CCR2	XM_541906	chemokine (C-C motif) receptor 2
CCR4	NM_001003020	chemokine (C-C motif) receptor 4
CCR5	NM_001012342	chemokine (C-C motif) receptor 5
CCR7	XM_548131	chemokine (C-C motif) receptor 7
CCR9	XM_541909	chemokine (C-C motif) receptor 9
CD274	XM_541302	CD274 molecule
CSF1	XM_849507	colony stimulating factor 1 (macrophage)
CSF2	NM_001003245	colony stimulating factor 2 (granulocyte-macrophage)
CSF3	XM_845213	colony stimulating factor 3 (granulocyte)
CTLA4	NM_001003106	cytotoxic T-lymphocyte-associated protein 4
CXCL10	NM_001010949	chemokine (C-X-C motif) ligand 10
CXCL11	XM_003640114	chemokine (C-X-C motif) ligand 11
CXCL12	NM_001128097	chemokine (C-X-C motif) ligand 12
CXCL5	XM_849650	chemokine (C-X-C motif) ligand 5
CXCR1	XM_536065	chemokine (C-X-C motif) receptor 1
CXCR2	NM_001003151	interleukin 8 receptor, beta
CXCR3	NM_001011887	chemokine (C-X-C motif) receptor 3
CXCR4	NM_001048026	chemokine (C-X-C motif) receptor 4
CXCR5	XM_546496	chemokine (C-X-C motif) receptor 5
EGF	NM_001003094	epidermal growth factor
EGFR	XM_533073	epidermal growth factor receptor
FOXP3	NM_001168461	forkhead box P3
GZMA	XM_544335	granzyme A (granzyme 1, cytotoxic T-lymphocyte-associated serine esterase 3)
GZMB	XM_547752	granzyme B (granzyme 2, cytotoxic T-lymphocyte-associated serine esterase 1)
HIF1A	XM_537471	hypoxia inducible factor 1, alpha subunit (basic helix-loop-helix transcription factor)
IDO1	XM_532793	indoleamine 2,3-dioxygenase 1
IFNG	NM_001003174	interferon gamma
IGF1	XM_848024	insulin-like growth factor 1 (somatomedin C)
IL10	NM_001003077	interleukin 10
IL12A	NM_001003293	interleukin 12A (natural killer cell stimulatory factor 1, cytotoxic lymphocyte maturation factor 1, p35)
IL12B	NM_001003292	interleukin 12B (natural killer cell stimulatory factor 2, cytotoxic lymphocyte maturation factor 2, p40)
IL13	NM_001003384	interleukin 13
IL15	XM_533281	interleukin 15
IL17A	NM_001165878	interleukin 17A
IL1A	NM_001003157	interleukin 1, alpha
IL1B	NM_001037971	interleukin 1, beta
IL1R1	XM_538449	interleukin 1 receptor, type I
IL2	NM_001003305	interleukin 2
IL22	XM_538274	interleukin 22

continued

Table E2. List of 89 Genes of Interest That Were Associated with Inflammation and Cancer *(continued)*

Gene Symbol	RefSeq No.	Gene Name
IL23A	XM_538231	interleukin 23, alpha subunit p19
IL4	NM_001003159	interleukin 4
IL5	NM_001006950	interleukin 5 (colony-stimulating factor, eosinophil)
IL6	NM_001003301	interleukin 6 (interferon, beta 2)
IRF1	XM_538621	interferon regulatory factor 1
MYC	NM_001003246	v-myc myelocytomatosis viral oncogene homolog (avian)
MYD88	XM_534223	myeloid differentiation primary response gene (88)
NFKB1	NM_001003344	nuclear factor of kappa light polypeptide gene enhancer in B-cells 1
NOS2	NM_001003186	nitric oxide synthase 2, inducible
PDCD1	XM_543338	programmed cell death 1
PTGS2	NM_001003354	prostaglandin-endoperoxide synthase 2 (prostaglandin G/H synthase and cyclooxygenase)
SPP1	XM_535649	secreted phosphoprotein 1
STAT1	XM_545571	signal transducer and activator of transcription 1, 91kDa
STAT3	XM_548090	signal transducer and activator of transcription 3 (acute-phase response factor)
TGFB1	NM_001003309	transforming growth factor, beta 1
LAMP1	XM_534193	Lysosomal Associated Membrane Protein 1
TLR2	NM_001005264, XM_005628829	toll-like receptor 2
TLR3	XM_540020	toll-like receptor 3
TLR4	NM_001002950	toll-like receptor 4
TLR7	NM_001048124	toll-like receptor 7
TLR9	NM_001002998	toll-like receptor 9
TNF	NM_001003244	tumor necrosis factor
IL18	NM_001003169	interleukin 18 (interferon-gamma-inducing factor)
FASLG	XM_547461	Fas ligand (TNF superfamily, member 6)
CXCL8	NM_001003200	interleukin 8
APLNR	XM_540616	apelin receptor
JAK1	XM_536679	Janus kinase 1
JAK2	XM_541301	Janus kinase 2
ICAM1	XM_542075	intercellular adhesion molecule 1
IL2RA	NM_001003211	interleukin 2 receptor, alpha
CD244	XM_545761	CD244 molecule, natural killer cell receptor 2B4
CCL13	NM_001003966	chemokine (C-C motif) ligand 13
CD209	NM_001130832	CD209 molecule
TBX21	XM_548164	T-box 21
NCR1	XM_849055	natural cytotoxicity triggering receptor 1
IL21R	XM_844902	interleukin 21 receptor
IL1R2	XM_538451	interleukin 1 receptor, type II
PDCD1LG2	XM_847012	programmed cell death 1 ligand 2
TNFRSF4	XM_546720	tumor necrosis factor receptor superfamily, member 4
HPRT1	NM_001003357	hypoxanthine phosphoribosyltransferase 1
GAPDH	NM_001003142	glyceraldehyde-3-phosphate dehydrogenase
ACTB	NM_001195845	actin, beta
GDC	–	genomic DNA control
PPC	–	positive PCR control
RTC	–	reverse transcription control
NTC	–	no template control